Observations of Infrared Sea Surface Temperature and Air–Sea Interaction in Hurricane Edouard (2014) Using GPS Dropsondes

JUN A. ZHANG

NOAA/Atlantic Oceanographic and Meteorological Laboratory/Hurricane Research Division, and Cooperative Institute for Marine and Atmospheric Studies, University of Miami, Miami, Florida

JOSEPH J. CIONE AND EVAN A. KALINA

NOAA/Atlantic Oceanographic and Meteorological Laboratory/Hurricane Research Division, Miami, Florida, and NOAA/Earth System Research Laboratory/Physical Sciences Division, Boulder, Colorado

ERIC W. UHLHORN

AIR Worldwide, Boston, Massachusetts

TERRY HOCK

Earth Observing Laboratory, National Center for Atmospheric Research, Boulder, Colorado

JEFFREY A. SMITH

NOAA/Aircraft Operations Center, MacDill Air Force Base, Florida

(Manuscript received 25 October 2016, in final form 3 April 2017)

ABSTRACT

This study highlights infrared sensor technology incorporated into the global positioning system (GPS) dropsonde platforms to obtain sea surface temperature (SST) measurements. This modified sonde (IRsonde) is used to improve understanding of air–sea interaction in tropical cyclones (TCs). As part of the Sandy Supplemental Program, IRsondes were constructed and then deployed during the 2014 hurricane season. Comparisons between SSTs measured by collocated IRsondes and ocean expendables show good agreement, especially in regions with no rain contamination. Surface fluxes were estimated using measurements from the IRsondes and AXBTs via a bulk method that requires measurements of SST and near-surface (10 m) wind speed, temperature, and humidity. The evolution of surface fluxes and their role in the intensification and weakening of Hurricane Edouard (2014) are discussed in the context of boundary layer recovery. The study's result emphasizes the important role of surface flux–induced boundary layer recovery in regulating the low-level thermodynamic structure that is tied to the asymmetry of convection and TC intensity change.

1. Introduction

Tropical cyclones (TCs) interact with the ocean through the air–sea interface, gaining energy in the form of enthalpy fluxes, and transferring momentum to the ocean through waves and currents. An improved knowledge of mechanisms underlying the air–sea interface is essential for interpreting dynamic and thermodynamic processes in TCs, and hence for improving numerical models with realistic prognostic capabilities for forecasting or simulating TCs (e.g., Bender et al. 2007; Davis et al. 2008; Kim et al. 2014; Zhang et al. 2015). Previous studies have demonstrated the important role of air–sea interaction, and in particular the sea surface temperature as it relates to forecasting TC track and intensity (Byers 1944; Malkus and Riehl 1960; Miller 1958; Palmen 1948; Shay et al. 1992, 2000; Zhu and Zhang 2006; Wu et al. 2007, 2008; Chen et al. 2007; Lin et al. 2005, 2009a,b; Knaff et al. 2013;

Denotes content that is immediately available upon publication as open access.

Corresponding author: Dr. Jun Zhang, jun.zhang@noaa.gov

DOI: 10.1175/JTECH-D-16-0211.1

Halliwell et al. 2015; Rogers et al. 2015). Emanuel (1986, 1988) noted that the maximum potential intensity (MPI) of a TC is primarily governed by the underlying sea surface temperature (SST). Previous studies have also shown that surface flux parameterizations linked to the SST are critical for accurately simulating TC intensity and structure (Emanuel 1995; Braun and Tao 2000; Nolan et al. 2009a,b; Smith and Thomsen 2010; Bryan 2012; Green and Zhang 2014; Ming and Zhang 2016).

Air–sea surface fluxes are important for TC simulations because they are key boundary conditions for numerical models. However, direct measurement of surface fluxes in strong wind conditions has proven to be very difficult (Moss 1978; Moss and Merceret 1976; Black et al. 2007; French et al. 2007; Drennan et al. 2007; Zhang et al. 2008; Zhang 2010a; Zhang et al. 2011). This is mainly due to the severe safety risks associated with manned aircraft and the inability of properly outfitted fixed ocean platforms to survive in strong tropical cyclones. Thus, air–sea fluxes are usually computed through a bulk method, using exchange coefficients and more easily measured mean quantities. When the SST and near-surface (10 m) temperature (T_{10}), humidity (q_{10}), and wind speed (U_{10}) are measured, surface heat (H) and moisture (E) fluxes can be estimated through

$$H = \rho c_p C_h U_{10}(\mathrm{SST} - T_{10}), \tag{1}$$

$$E = \rho L_v C_e U_{10}(q_0 - q_{10}), \tag{2}$$

where C_h and C_e are the exchange coefficients for sensible heat and latent heat transfer, respectively; ρ is the air density; q_0 is the absolute humidity at the sea surface that is calculated using SST and surface pressure assuming saturation; c_p is the specific heat capacity of air at constant pressure; and L_v is the latent heat of evaporation.

In TCs, simultaneous observations of q_{10}, T_{10}, U_{10}, and SST are typically obtained by surface buoys (Cione et al. 2000; Cione and Uhlhorn 2003; Cione et al. 2013; Jaimes et al. 2015; Jaimes and Shay 2009). Alternatively, global positioning system (GPS) dropsondes and airborne expendable bathythermographs (AXBT) dropped simultaneously from the research aircraft can provide measurements of all of these variables necessary for flux calculations. However, the utility of the AXBT to routinely provide SST is limited due to aircraft weight and balance restrictions. SST sensors installed on the much smaller dropsondes (IRsonde) provide an attractive alternative to obtain SSTs in high-wind, cloud-covered hurricane conditions. The utility of this approach using the IRsonde concept has been demonstrated with the High-Definition Sounding System (HDSS) expendable digital dropsode (XDD) for low-wind, relatively quiescent conditions (Black et al. 2017).

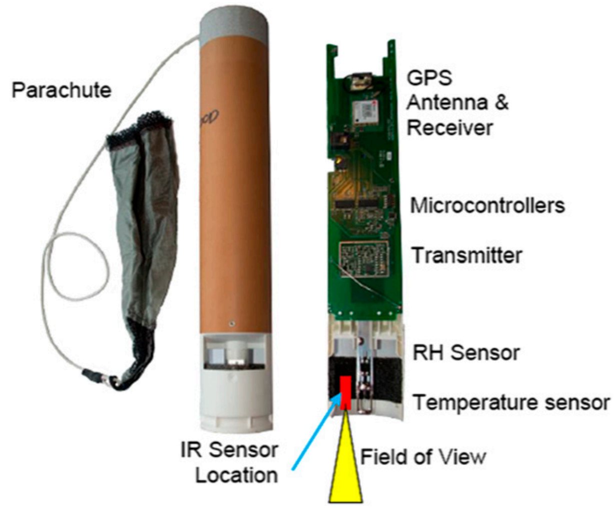

FIG. 1. A schematic of the (left) IRsonde appearance and (right) inside view of the sensors of the IRsonde.

As part of the Sandy Supplemental Program support received by the National Oceanic and Atmospheric Administration (NOAA), new technologies were developed to improve air–sea flux observations and to provide validation for operational coupled hurricane models. Based on a prototype of the Airborne Vertical Atmospheric Profiling System (AVAPS) associated with the GPS dropsonde, an infrared (IR) sensor was incorporated into AVAPS that provides remote measurements of SST. The IRsonde presented here was modified from the standard Vaisala RD94 dropsonde[1] that was developed by the National Center for Atmospheric Research (NCAR). During the 2014 hurricane season, IRsondes were carried and released by NOAA's Lockheed WP-3D Orion (P3) aircraft. Most of the IRsondes were released in Hurricane Edouard (2014). This study evaluates the performance of the SST measurements obtained from the IRsonde and compares these values with measurements from AXBTs that were deployed nearby. In addition, surface flux calculations using SSTs from the IRsonde via the bulk aerodynamic equations will be presented.

2. Description of IRsonde and SST comparison

To obtain SST measurements, the Melexis infrared thermometer and infrared sensor were integrated with a standard GPS dropsonde to create the IRsonde (Fig. 1). According to manufacturer specifications, the Melexis

[1] This type of dropsonde is different from the MiniSonde reported by Black et al. (2017).

sensor has an accuracy of ±0.5° to 1°C. It measures temperatures between −70° to 380°C with a resolution of 0.02°C. The wavelength pass band optical filter ranges from 5.5 to 15 μm. It senses the radiation from all gases in the atmosphere. Before the sensor was installed in the IRsonde, it was calibrated in front of a blackbody with an emissivity close to 1 using a calibration facility at the NCAR calibration laboratory. The SST measured by the IRsonde was also tested by dropping the sonde from NOAA's G-IV aircraft in the vicinity of a NOAA National Data Buoy Center (NDBC) buoy (Hock 2014), showing good agreement (i.e., errors within 0.5°C). Of note, in precipitation, two IRsondes deployed near a Gulf of Mexico NDBC buoy measured SSTs that were ~2°C cooler than the buoy observation; similar results were found in our study (shown later).

The infrared sensor measures the sea surface skin temperature from every altitude. Figure 2 shows an example of the SST measured by the IRsonde as a function of altitude, indicating that the SST measurements attenuate at high altitudes. Also shown in Fig. 2 are the vertical profiles of temperature and dewpoint temperature. Because the infrared sensor samples through its entire descent, the apparent temperature tends to increase in moist conditions as the sonde descends, due to the decreasing depth of the intervening, radiatively colder atmosphere (Fig. 2). Of note, the downward-pointing IR sensor is also weakly affected by reflection from the sea surface. The noise in the data may be due to the sensor facing at various angles as it descends.

The SST is taken to be the maximum value in the lowest 100 m of the profile. Using a height threshold of 50 m gives similar results as using 100 m; 100 m was chosen as the threshold for the purpose of enlarging the data sample size, as dropsondes tend to splash at a GPS-estimated altitude of 50 m or lower. Another method was used by Black et al. (2017) to estimate SST by linearly extrapolating the data to the surface using the SST profile in the lowest 100 m. Barnes and Powell (1995) and Drennan et al. (2007) also used the extrapolation method to find the SST using data collected by the PRT-5 radiometer aboard the P3 aircraft. We found that the results from our method do not differ significantly from those provided by the linear extrapolation method (not shown). The advantage of the IRsonde is that it provides measurements below 100 m, which cannot be easily achieved by manned aircraft in TCs. The accuracy of the IRsonde-measured SST increases with decreasing distance to the sea surface, since the atmospheric attenuation becomes smaller with decreasing height.

To evaluate the accuracy of the SST measurements by the IRsonde in hurricane conditions, we use SSTs measured by AXBTs that were simultaneously dropped with the IRsondes. Figure 3 shows a comparison of the SST measured by the IRsonde and the AXBTs. A total of 30 IRsonde–AXBT pairs were obtained in Hurricane Edouard (2014). The comparison of IRsonde SSTs with AXBT SSTs indicates a statistically significant bias of −0.62°C (95% confidence) with a root-mean-square error of 1.24°C. Outliers with 2°–3°C differences contribute to a fairly weak correlation (r^2 = 0.472; Fig. 3a). Detailed evaluation of the radar reflectivity data reveals that the IRsondes that have relatively large cool SST biases compared to AXBT measurements that were dropped in rain (i.e., 1.5-km radar reflectivity > 20 dBZ). These IRsondes were mainly dropped in the eyewall and at the midpoints of the flight pattern shown in Fig. 4. A comparison of SST measured by the IRsonde without rain contamination and collocated AXBTs (16 pairs) shows a much improved correlation (r^2 = 0.902) and a very small bias of 0.0745°C (Fig. 3b). The root-mean-square error is also reduced to 0.472°C. This result suggests that the IRsondes can be successfully used to measure SSTs in rain-free to light rain conditions in hurricanes. All of the IRsonde-measured SSTs made in the hurricane eye show very good agreement with the SST measurements made by AXBTs. Thus, it is recommended that IRsonde-measured SSTs in the eye be used to represent SST conditions within the eyewall during future TC field campaigns.

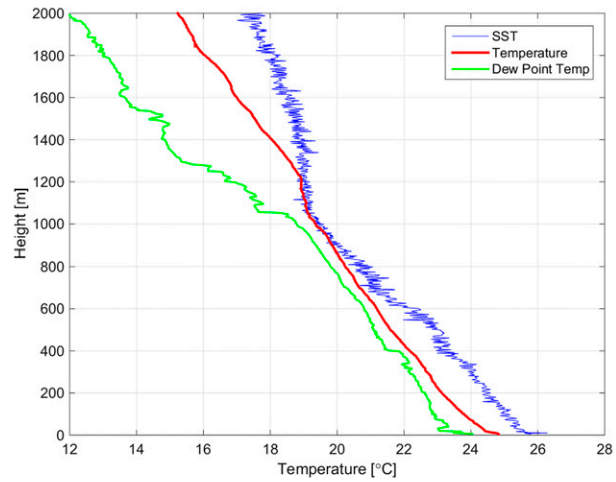

FIG. 2. An example of IRsonde-measured vertical profiles of temperature, dewpoint temperature, and IR temperature.

3. Observations of air–sea interaction in Hurricane Edouard using IRsondes and AXBTs

A total of 57 IRsondes were dropped in Hurricane Edouard (2014) on 3 consecutive days from 15 to 17 September. Edouard developed from a tropical wave

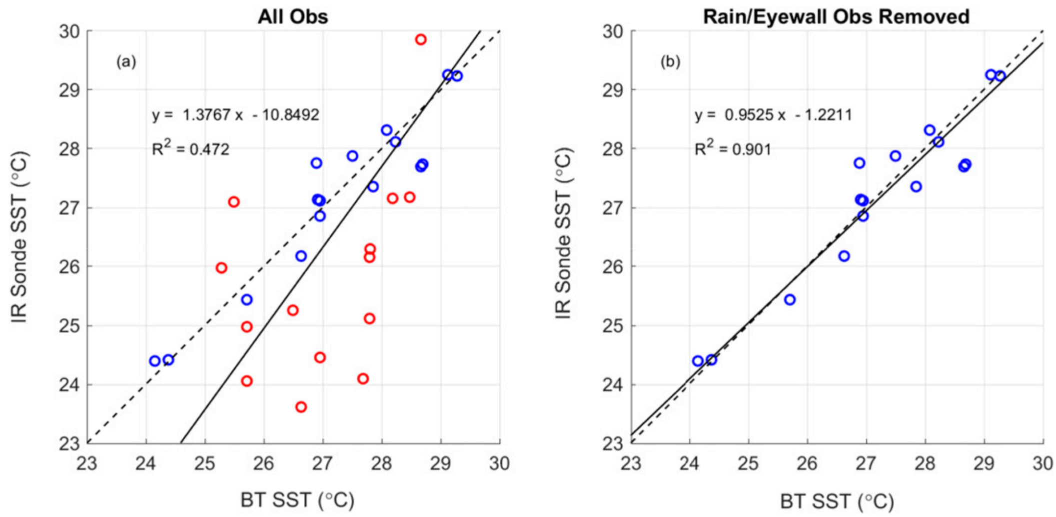

FIG. 3. Scatterplot of AXBT vs IRsonde SST (°C) for (a) 30 pairs of collocated measurements and (b) the 16 pairs without IRsondes in the eyewall and rain regions. Shown are the 1:1 ratio (dashed black line) and the best-fit linear regression (equation shown in upper left; solid black line). The correlation coefficient squared (R^2) is also shown. IRsondes dropped in heavy rain (red circles) and light to no rain (blue circles) regions.

that emerged from the west coast of Africa on 6 September 2014 (Stewart 2014) and became a tropical depression (TD6) on 11 September, approximately 1800 km east of the Caribbean Windward Islands. As TD6 continued on a northwest track, it was named Tropical Storm (TS) Edouard by the National Hurricane Center (NHC) on 12 September and further intensified into a hurricane early on 14 September. From 14 to 16 September, Edouard underwent steady intensification to its maximum intensity of 105 kt (1 kt = 0.51 m s^{-1}) at 1200 UTC16 September as it curved northward, becoming the first major hurricane in the Atlantic basin since Hurricane Sandy in 2012. Hurricane Edouard weakened just east of Bermuda and quickly recurved toward the northeast and east, degenerating into a remnant low by 19 September just west of the Azores Islands. Hurricane Edouard (2014) was extensively observed by manned aircraft, including two P3s and the NOAA G-IV (Rogers et al. 2016; Zawislak et al. 2016). Figure 4 shows the evolution of the maximum intensity of Edouard from the best track along with the time of each aircraft mission.

The flight tracks of the aforementioned aircraft on the 3 days of observations in Hurricane Edouard (2014) are shown in Figs. 5a–c. On each day, the observation time window spanned from 1200 to 1800 UTC. NOAA's P3 aircraft released the IRsondes. IRsonde and AXBT locations are shown in Fig. 5d in a storm-relative framework, with the colors representing the date of each observation. The data coverage on 15 September provides the best, highest density coverage. As such, a two-dimensional (2D) objective analysis designed to assess the asymmetry of surface fluxes during the intensification of Hurricane Edouard was possible on this date and will be provided in section 3b. Note that before the flux calculation, we corrected the IRsonde-measured SSTs in the eyewall region using the collocated AXBT data (if available) or by the adjacent IRsonde data in the eye if there was no AXBT observation available. Two IRsondes released at the midpoint of a radial leg measured cool-biased SST, where high radar reflectivity was observed and no AXBT was released. We corrected the SSTs of these two sondes by

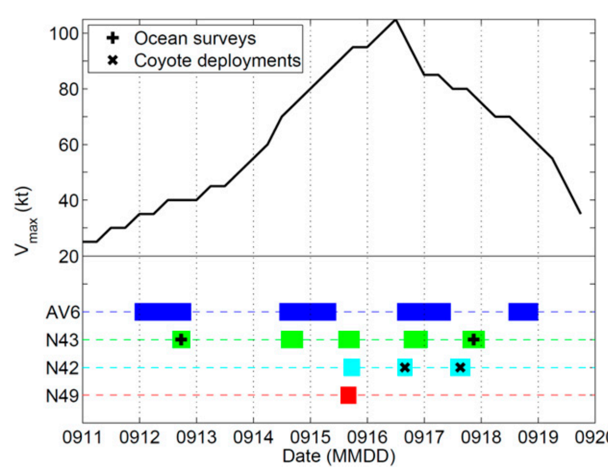

FIG. 4. Timeline of Edouard aircraft missions along with best-track intensity (Vmax, kt). Participating aircraft are the NASA Global Hawk (AV6), two NOAA WP-3Ds (N42, N43), and NOAA G-IV (N49). Note that the N43 flights on 12 and 17 Sep were ocean surveys in front of and behind the storm, respectively, and not in the storm.

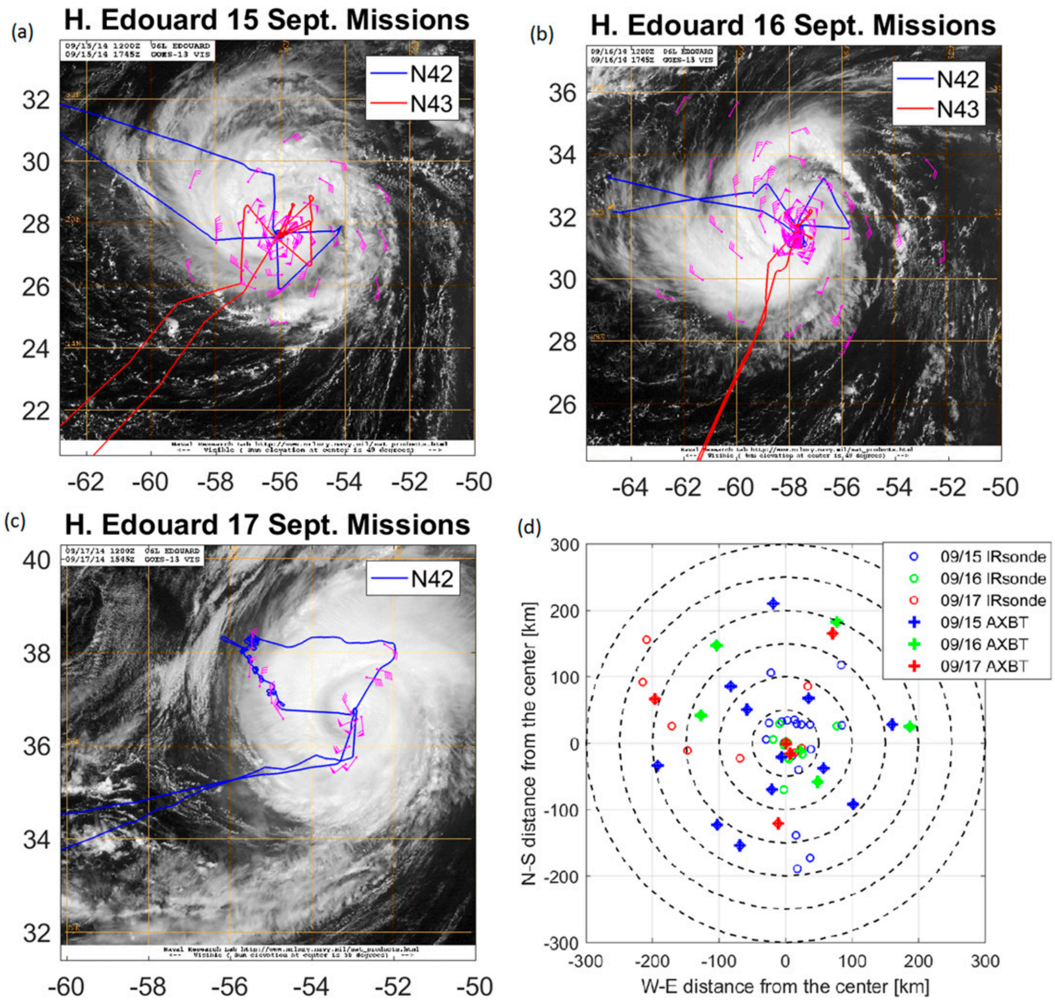

FIG. 5. Hurricane Edouard flight missions on 15–17 Sep. (a)–(c) Storm-relative locations of IRsondes (circles) and (d) AXBTs (pluses) are shown, with each color representing each day. Flight tracks are shown in a translating storm-relative coordinate system, centered on the storm. Near-surface GPS dropwindsonde wind barbs are shown in magenta, also at storm-center-relative locations. GOES visible satellite images (courtesy of NRL Monterey) are at approximate center time of missions.

linearly interpolating the SSTs used in the eye/eyewall and the end point.

a. Radial distribution of air–sea variables

Radial profiles of 10-m wind speed, air temperature, specific humidity, and sea surface temperature all measured by the IRsondes are shown in Figs. 6a–d. Here, the variables are plotted as a function of radius normalized by the radius of maximum winds (RMW; $r^* = r/\mathrm{RMW}$), determined from the Stepped Frequency Microwave Radiometer (SFMR) data (Zhang and Uhlhorn 2012). Again, the colors represent the dates that the observations were made. It is evident from Fig. 6a that the maximum 10-m wind speed decreased from $\sim$55 m s^{-1} on 15 September to 32 m s^{-1} on 17 September, indicating the weakening of Hurricane Edouard. The 10-m temperature (T_{10}) was found to decrease with radius to the storm center from the outer core to the eyewall region but to somewhat increase toward the center between the ambient environment and the outer core during all 3 days (Fig. 6b). This radial variation of T_{10} is consistent with buoy observations given by Cione et al. (2000, 2013) and dropsonde observations given by Barnes and Bogner (2001), indicating that the hurricane surface layer is not isothermal, contrary to what is assumed in the axisymmetric model used in previous theoretical studies (e.g., Emanuel 1986). The radial variation of q_{10} is also consistent with previous buoy observations given by Cione et al. (2000, 2013), showing an increasing trend with decreasing radius (Fig. 6b).

The quality-controlled SSTs measured by IRsondes and AXBTs as a function of normalized radius are also

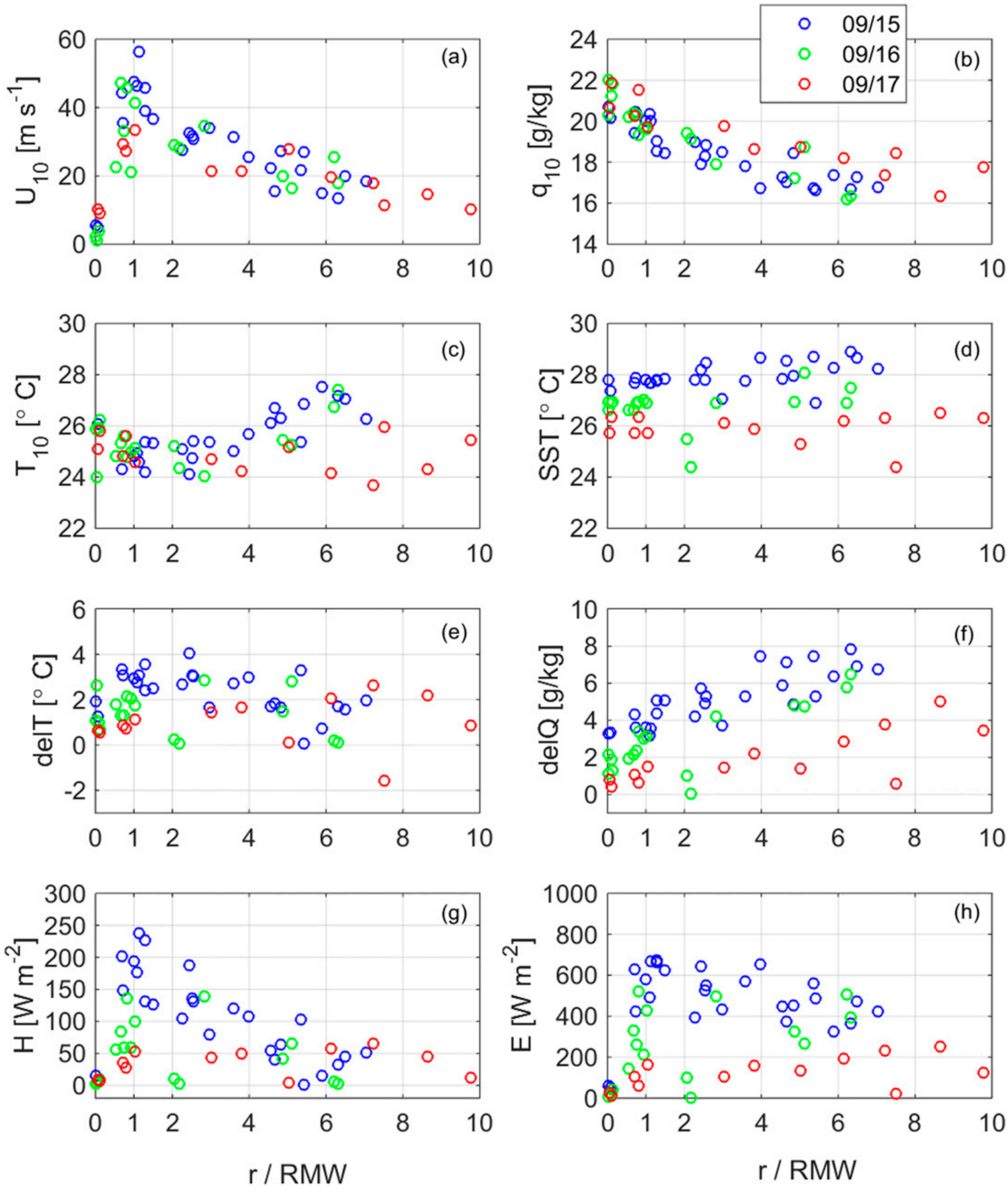

FIG. 6. Plots of (a) 10-m wind speed, (b) 10-m air temperature, (c) 10-m specific humidity, (d) SST, (e) air–sea contrast of temperature, (f) air–sea contrast of specific humidity, (g) sensible heat flux, and (h) latent heat flux, as a function of radius to the storm center that is normalized by the RMW at 10 m. Each color represents the date of observations: blue represents 15 Sep, green represents 16 Sep, and red represents 17 Sep.

shown in Fig. 6d. The ambient (>150 km) SST decreased from 15 to 17 September. On average, the ambient SST was ~3°C cooler on 17 September than on 15 September, as the storm moved north of 30° latitude. The in-storm maximum SST cooling estimated by subtracting the minimum SST from the maximum ambient SST is 1.7°, 4.2°, and 0.8°C from 15 to 17 September, respectively. The ambient SSTs are near or below 26°C on 17 September, which is the minimum threshold commonly assumed to be conducive to hurricane development (Byers 1944; Miller 1958; Cione 2015). It is observed from the best track that the storm weakened substantially after it moved into the colder water on 17 September, indicating the influence of air–sea coupling on hurricane intensity. Compared to the climatology based on buoy data developed by Cione and Uhlhorn (2003), the observed inner-core SST cooling is significantly larger on 16 September. However, compared to satellite observations, the IRsonde observed in-storm

SST cooling comparable to the poststorm SST cooling of ~4°–7°C shown in the National Hurricane Center's annual report of Hurricane Edouard (Stewart 2014). This large cooling may be related to the shallow mixed layer as the storm moved into cooler water in the higher latitudes (>25°N). The inner-core SST cooling is smaller on 17 September compared to that on 15 and 16 September and is consistent with Cione and Uhlhorn (2003), who found from extensive buoy observations that the storm-induced SST cooling is smaller when the ambient SST is cool and the latitude is high.

Radial profiles of the air–sea contrast of temperature and humidity between the air at 10 m and the sea surface are shown in Figs. 6e and 6f, respectively. Overall, the air–sea temperature contrast is similar during the 3 days. The majority of the data (>95%) have positive air–sea temperature contrast (i.e., SST $-$ T_{10}). Later we show that the one measurement of negative air–sea contrast was mainly due to the SST cooling in the right-rear quadrant of the storm relative to the storm motion. The air–sea humidity contrast generally decreased with decreasing radius during the 3 days, consistent with results from Cione et al. (2013) based on extensive buoy observations. The magnitude of the air–sea humidity contrast was the largest on 15 September when the storm was intensifying, while it was the smallest on 17 September when the storm was weakening. The larger humidity contrast drove larger latent heat fluxes, as shown later. The air–sea humidity contrast is much smaller on 17 September than that on the other 2 days, which likely contribute to the weakening of Edouard.

Sensible heat and latent heat fluxes calculated using the bulk method are shown in Figs. 6g and 6h, respectively. Here, we used $C_h = C_e = 0.0012$ following Zhang et al. (2008), Haus et al. (2010), and Bell et al. (2012). The magnitudes of both the latent heat flux and the sensible heat flux were substantially larger on 15 September than on the other 2 days. In particular, the magnitude of the latent heat flux on 15 September was nearly 3 times greater than the values estimated on 16 and 17 September. Surface wind speed differences between 15 and 17 September also contributed to the large surface flux difference. Conversely, the difference in the latent heat flux between 15 and 16 September was mainly due to the difference in the air–sea humidity contrast, since the wind speed difference was relatively small between these 2 days. It is noted that the magnitude of the latent heat flux was correlated with the rate of intensity change of Hurricane Edouard.

b. 2D analyses of enthalpy fluxes

To investigate the asymmetric distribution of surface fluxes, we constructed a 2D objective analysis of the data using the same method as Dolling and Barnes (2014). This method uses the piecewise cubic spline to fit the data into equally spaced grids while preserving values from the original observations. The analysis covers only the area where observations were made (i.e., no extrapolation to locations outside of the observed area was made). Details of this method are provided in Dolling and Barnes (2014).

Horizontal views of the 10-m temperature, specific humidity, and SST are shown in Fig. 7 for the 3 days of observations. For the purpose of clearly showing the location of SST cooling, the data were rotated relative to the storm motion direction, which points to the top of the figure. It is seen again that the data coverage is the best on 15 September, so that the asymmetric structure can be fully explored within ~150-km radius (i.e., ~5 times the RMW). It is evident from Fig. 7a that the coolest SSTs on 15 September are located in the right-rear quadrant, consistent with previous studies (e.g., Price 1981; Price et al. 1994; D'Asaro et al. 2007; Black et al. 2007; Chen et al. 2007; Uhlhorn and Shay 2008; Yablonsky and Ginis 2009; Cione et al. 2013; Cione 2015). With limited data coverage on 16 September, the coolest SSTs were found on the right side of the storm. Figures 6a–c indicate that SSTs cooled ahead of the storm from 15 through 17 September, which is consistent with expectations given the storm's northward propagation.

On 15 September, the 10-m air temperature was the warmest in the ambient environment. The air temperature decreased as a function of decreasing radius toward the storm center to a minimum in the eyewall region before increasing with decreasing radius in the eye (Fig. 7d). Of note, the SST in the eye is typically close to that in the eyewall based on climatology (Cione et al. 2000); here, the observed SST difference between the eye and eyewall may be due to the sampling variability. This trend of variation in the air temperature was also observed on 16 and 17 September (Figs. 7e and 7f). In the inner-core region ($r^* < 3$), the air was cooler on the left side of the storm than on the right side of the storm on 15 September. The 10-m humidity structure was similar during the 3 days and shows that the humidity increased from the large radii to the storm center. On 15 September, when data coverage was good, it shows that the left side of the storm was drier than the right side of the storm. In the eyewall region, the right-front quadrant was the most humid. Of note, the environmental wind shear[2] direction was aligned with the storm motion direction on 15 September, such that the right-front quadrant corresponded to the downshear right

[2] The shear information used in this study was based on the Statistical Hurricane Intensity Prediction Scheme (SHIPS) model (DeMaria et al. 2005; Kaplan et al. 2015).

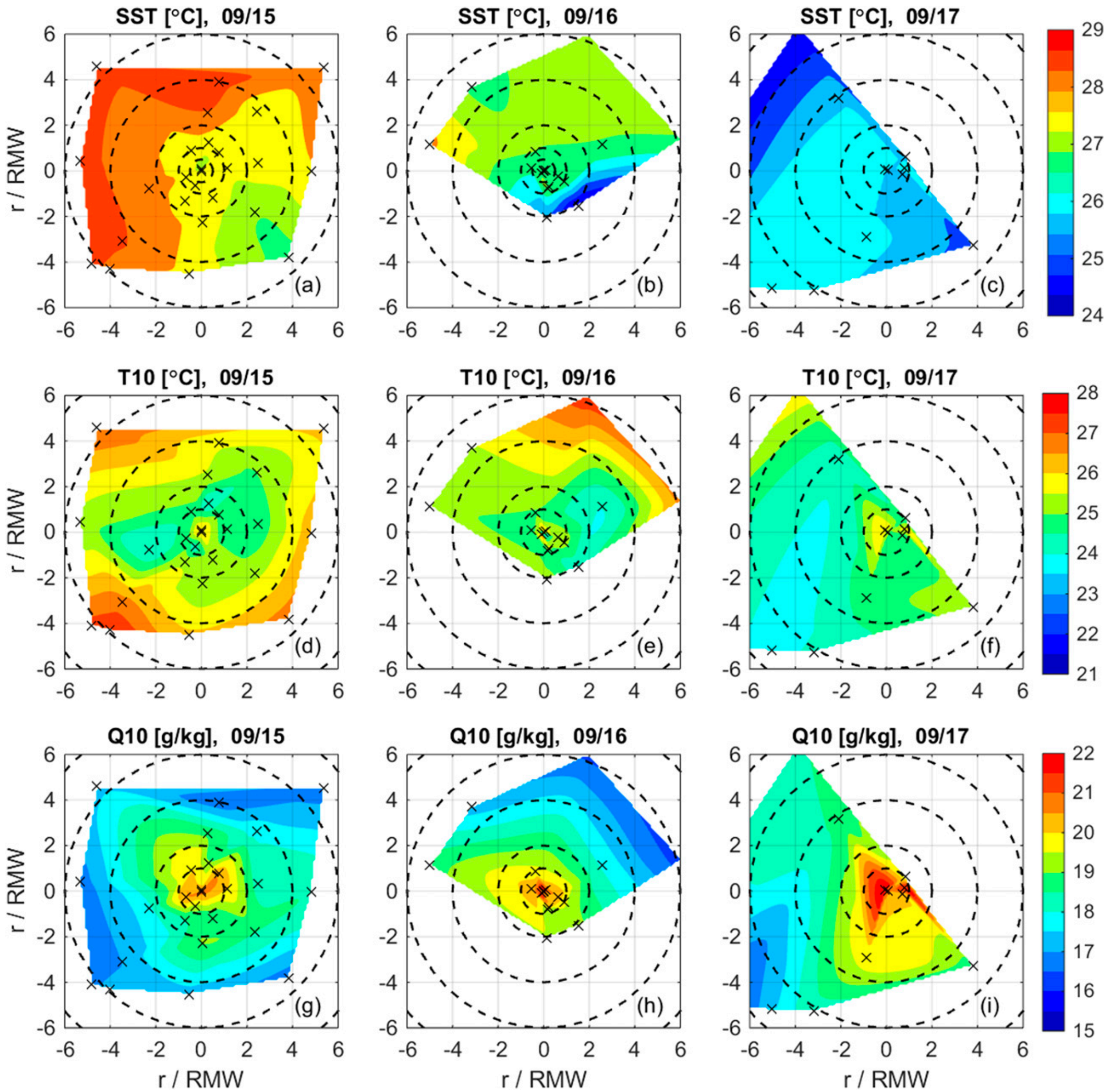

FIG. 7. (top) The 2D analysis of SST, (middle) T_{10}, and (bottom) Q_{10}. (left to right) Results from 15 to 17 Sep, respectively. Note that the data are rotated relative to the storm motion direction to the top of the figure. Location of IRsonde used in the analysis is shown (black x).

quadrant where the convection was initiated. Later, we show that the asymmetry in the equivalent potential temperature θ_e in the inner-core region resembles that of the composite analysis given by Zhang et al. (2013). This θ_e pattern is also similar to that of Hurricane Bonnie (1998), documented by Schneider and Barnes (2005), and Hurricane Guillermo (1998), documented by Sitkowski and Barnes (2009).

Figure 8 shows the horizontal view of surface sensible heat fluxes (upper panels), air–sea temperature contrast (middle panels), and 10-m wind speed (lower panels) for 15–17 September, from the left to right columns, respectively. It appears that the asymmetric pattern in the sensible heat flux is close to that of the air–sea temperature contrast as well as the SST. For instance, on 15 September, the smallest sensible heat flux was collocated with the largest SST cooling seen at the right-rear quadrant where the air–sea temperature contrast was also the smallest. The largest positive sensible heat flux on 15 September was located in the right-front quadrant of the storm in the eyewall where the air–sea contrast was large and the surface wind speed was the

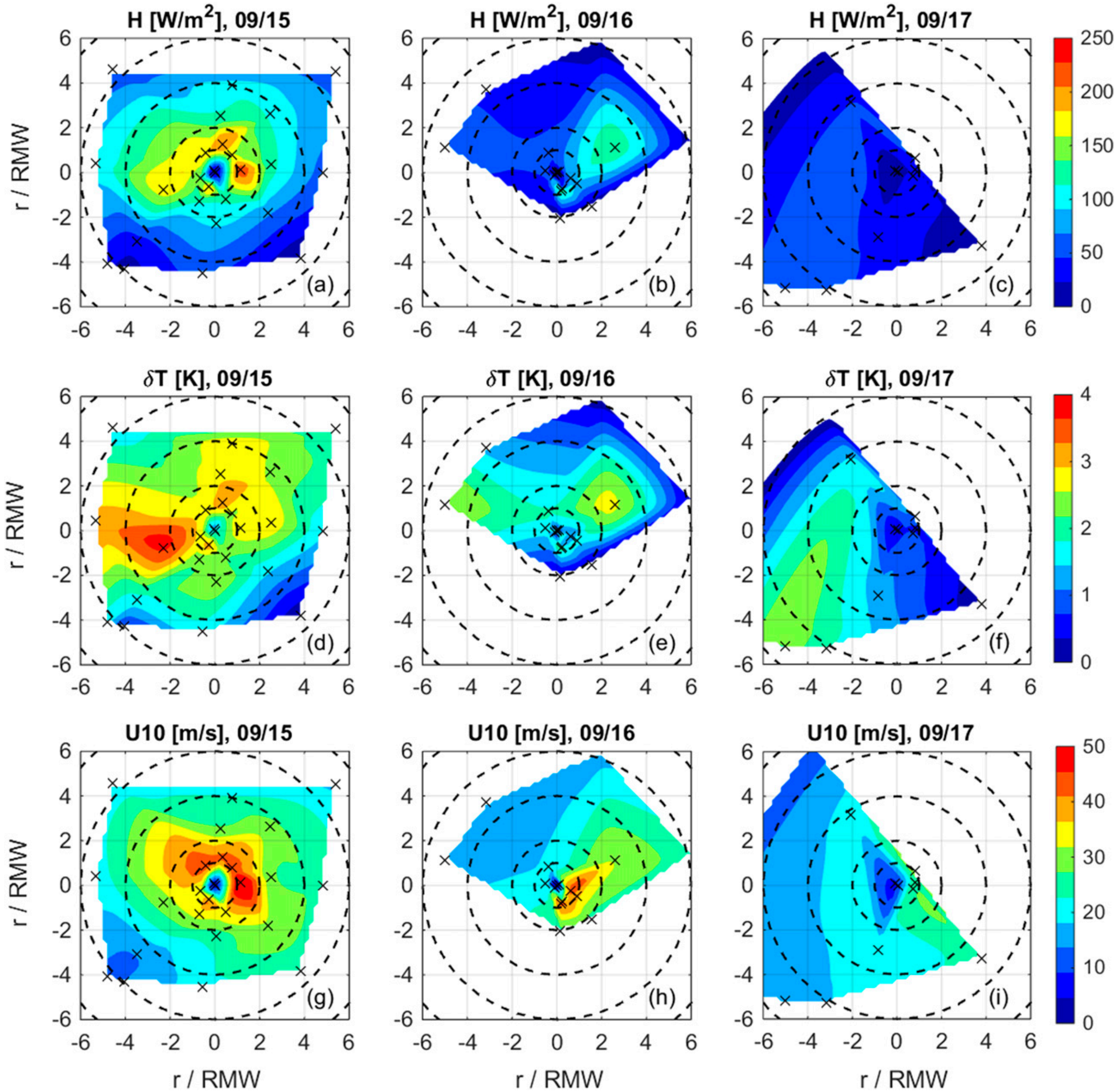

FIG. 8. (top) The 2D analysis of H, (middle) air–sea temperature contrast δT, and (bottom) U_{10}. (left to right) Results from 15 to 17 Sep, respectively. Note that the data are rotated relative to the storm motion direction to the top of the figure. Location of IRsonde used in the analysis is shown (black x).

largest. On 16 September, the air–sea temperature contrast was close to zero in the eyewall region, which made the sensible heat flux very small, even though the surface wind speed was large. Of note, the surface wind speed asymmetry seen on 15 and 16 September is consistent with previous numerical and observational studies (e.g., Shapiro 1983; Kepert and Wang 2001; Uhlhorn et al. 2014). On 17 September, the magnitude of the sensible heat flux was very small ($<$20 W m^{-2}) due to the cool SST and weak surface wind speed.

The storm-relative latent heat fluxes estimated using the IRsonde data are shown in Fig. 9 for the 3 days of interest along with the air–sea humidity contrast and wind speed. The magnitude of the latent heat flux on 16 and 17 September is much smaller than that on 15 September in the inner-core region ($r^* < 3$). In particular, the majority ($>$80%) of latent heat flux is under 50 W m^{-2} on 17 September when the storm moved over the cool SST region, indicating that the available energy from the surface latent heat flux was too limited to

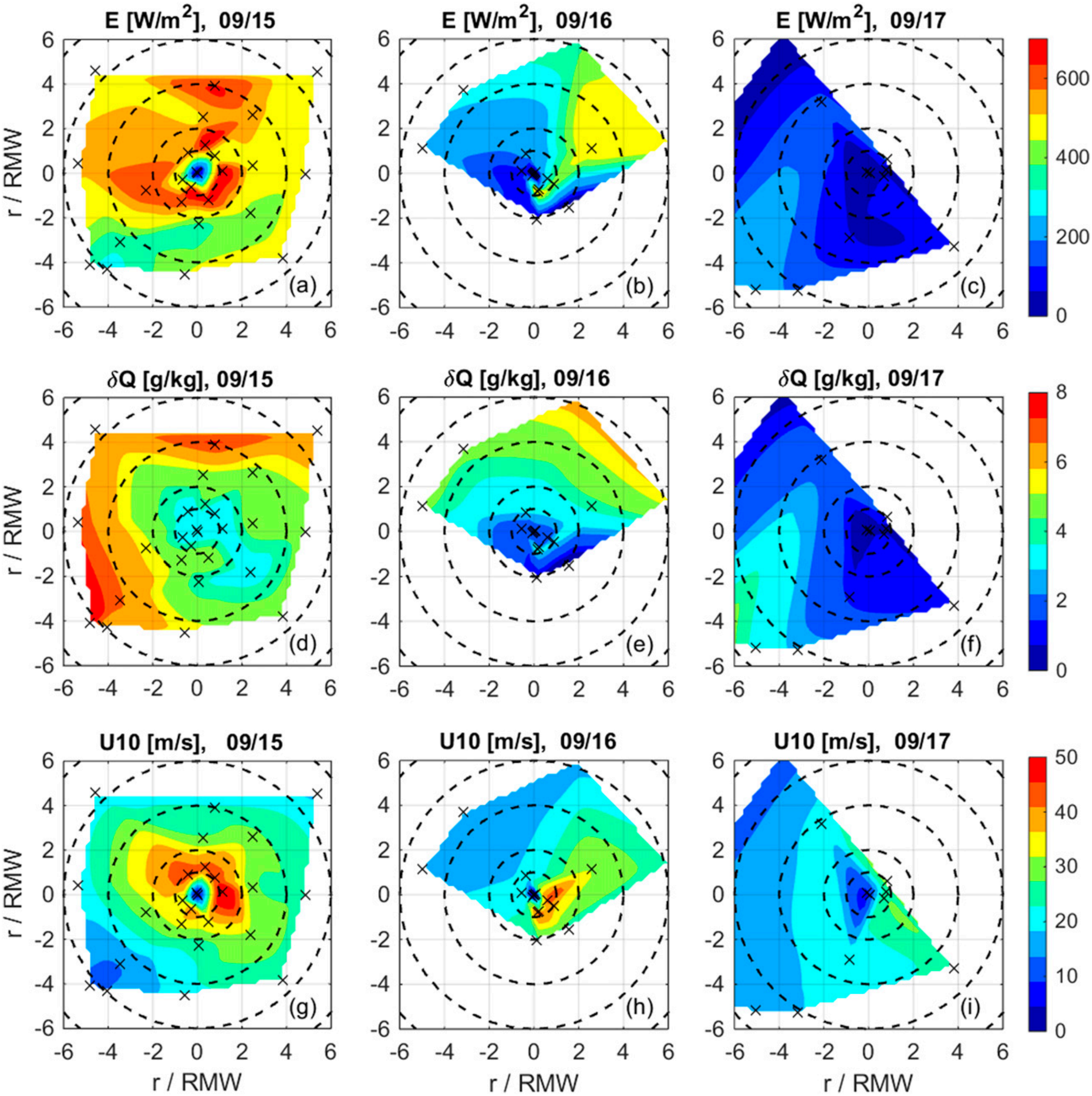

FIG. 9. (top) The 2D analysis of H, (middle) air–sea humidity contrast δlQ, and (bottom) U_{10}. (left to right) Results from 15 to 17 Sep, respectively. Note that the data are rotated relative to the storm motion direction to the top of the figure. Location of IRsonde used in the analysis is shown (black x).

support storm intensification. This result is consistent with the findings of Cione (2015) and may explain why the storm weakened on 16 and 17 September, especially on 17 September. The surface layer nearly reached equilibrium in humidity on 16 September, so the latent heat flux was shut down in the core of the storm even though the surface wind was large ($>40\,\mathrm{m\,s^{-1}}$). Of note, an eyewall replacement cycle that occurred on 16 September also contributed to the weakening of the storm. On 17 September, as the SST was cool, the latent heat flux was close to zero, which may be the reason for the storm weakening, given that the environmental wind shear remained steady ($\sim 7.5\,\mathrm{m\,s^{-1}}$) from 15 to 17 September.

The good data coverage on 15 September again allows us to explore the asymmetry of the latent heat flux (Fig. 9a). As expected, at large radii ($r^* > 3$), the largest latent heat flux was located at the front of the storm where the SST was the largest and the air–sea humidity

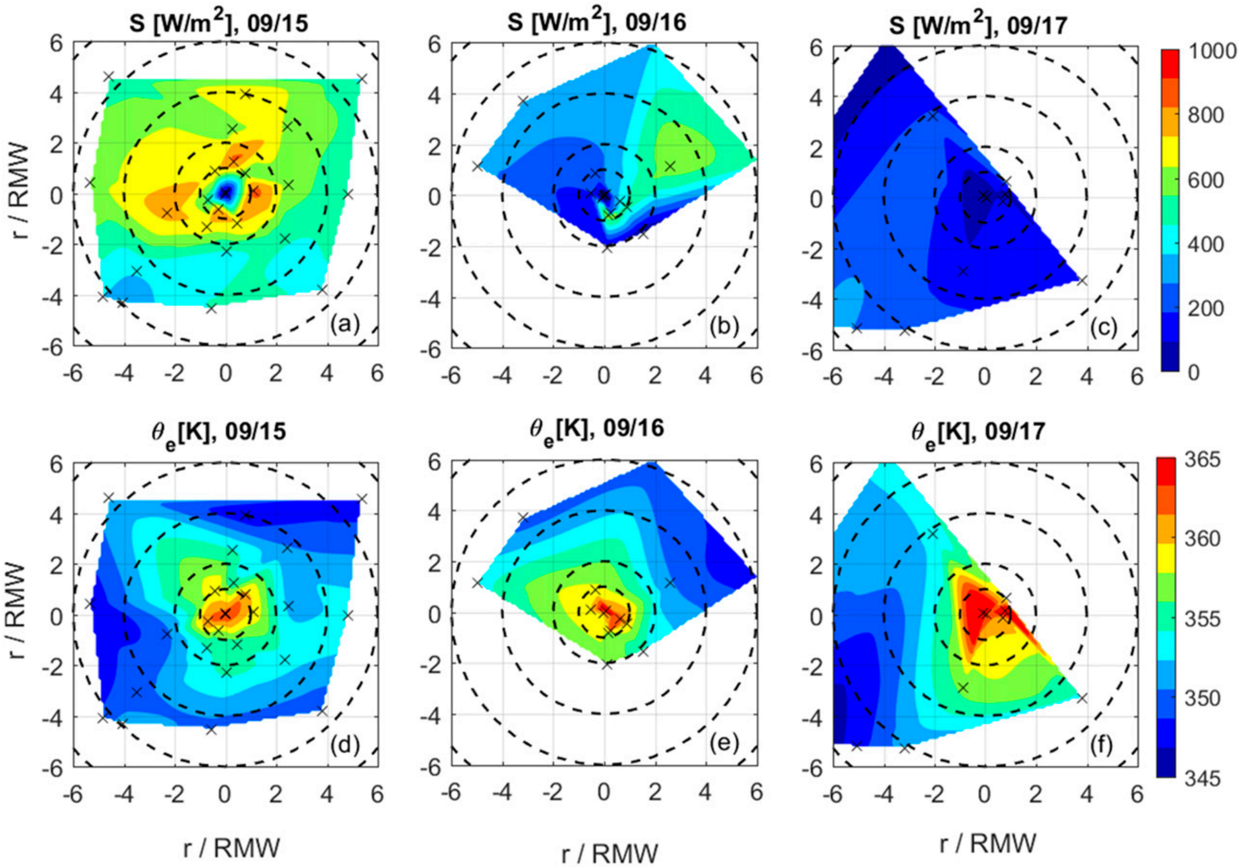

FIG. 10. (top) The 2D analysis of total S and (bottom) θ_e. (left to right) Results from 15 to 17 Sep, respectively. Note that the data are rotated relative to the storm motion direction to the top of the figure. Location of IRsonde used in the analysis is shown (black x).

contrast was also the largest, and the smallest latent heat flux was located in the right-rear quadrant where the SST cooling was the largest. In the eyewall region ($r^*\sim1$), the maximum latent heat flux was located in the right-front quadrant where the surface wind speed was the largest, although the air–sea humidity contrast was not the largest there. On 15 September, the air–sea humidity contrast, although small, did not reach equilibrium as on 16 and 17 September. This result (Figs. 8 and 9) suggests that the role of wind speed in inducing the surface fluxes is strongly tied to the air–sea thermodynamic equilibrium condition. The effect of surface wind speed on the surface enthalpy flux becomes larger only if the thermodynamic equilibrium condition is not reached. This result also suggests the thermodynamic equilibrium condition tends to occur during the storm weakening phase or, in fact, may be an important factor responsible for initiating the weakening process.

The total enthalpy fluxes S calculated by combining the sensible and latent heat fluxes during the 3 days are shown in Fig. 10, along with a 2D analysis of the 10-m θ_e. On 15 September, the magnitude of the enthalpy flux was as large as 900 W m^{-2} in the eyewall region ($0.75 < r^* < 1.25$), which is nearly an order of magnitude larger than that on 16 and 17 September. The smallest enthalpy heat flux was located in the right-rear quadrant, where the SST cooling was the largest on 15 September. With similar intensity on 15 and 16 September, the magnitude of θ_e in the storm center and the eyewall region was similar. However, the magnitude of the enthalpy flux was very different. Of note, the intensification rate was also very different between 15 and 16 September, as mentioned earlier, when the storm underwent intensification and weakening, respectively. This result indicates that air–sea enthalpy flux is a key variable that drives hurricane intensity change.

c. Boundary layer recovery due to surface flux

In addition to the abovementioned discussion that used 2D analyses in a storm-relative framework referenced to the storm motion direction, analyses of the enthalpy flux and θ_e were rotated relative to the environmental shear direction (Fig. 11). Here, only the inner-core region ($r^* <2$) is shown for 15 and 16 September. As mentioned earlier,

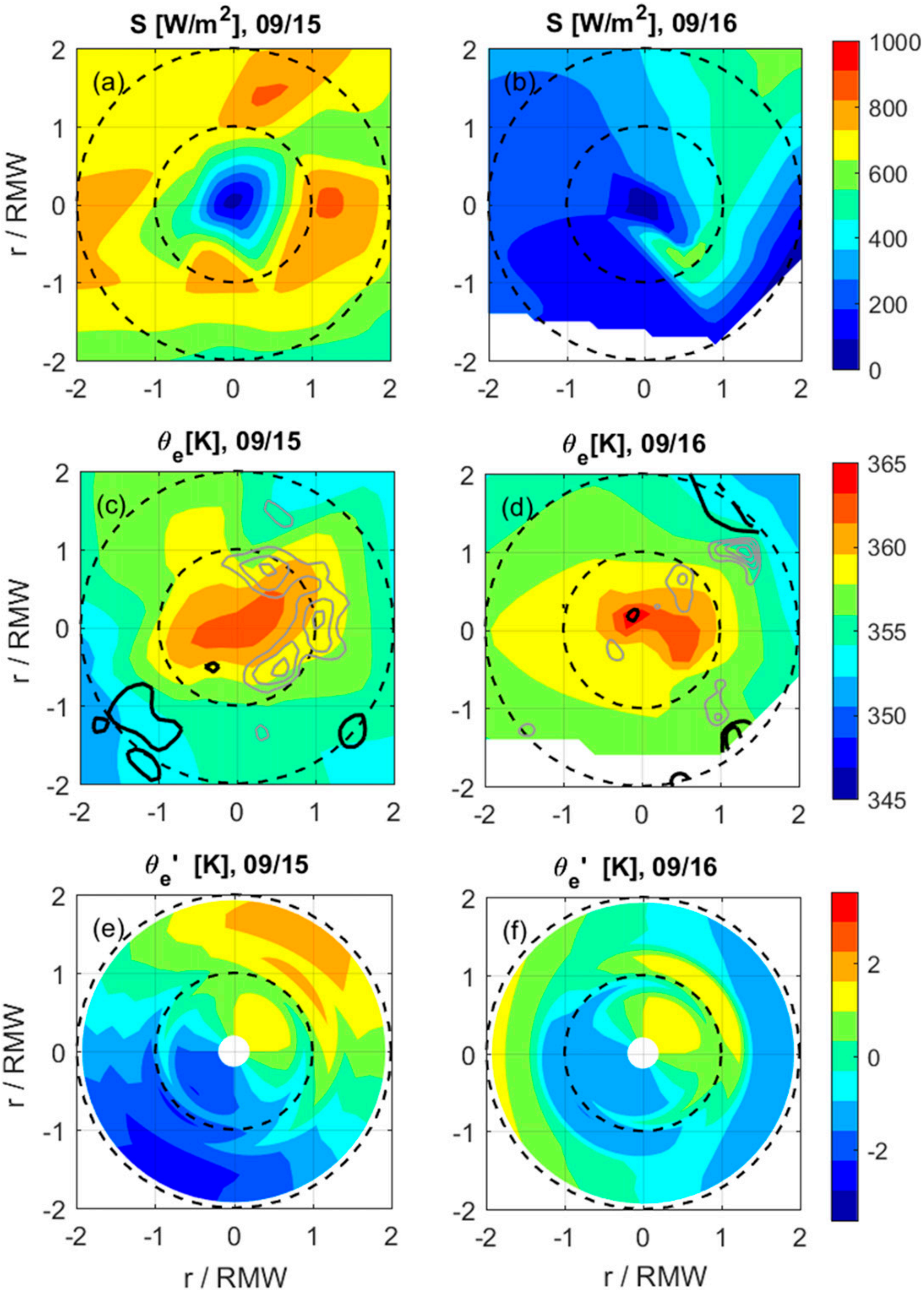

FIG. 11. Horizontal view of (top) S, (middle) θ_e at 50 m, and (bottom) wavenumber 0 + 1 component of θ_e. Results from (left) 15 and (right) 16 Sep. Note that the data are rotated relative to the environmental shear direction to the top of the figure. (c),(d) Vertical velocity from the Doppler radar data (contours) with downward motion (black contours) and upward motion (gray contours), and the contour interval is 0.2 m s^{-1}.

the shear direction was the same as the storm motion direction on 15 September. Thus, the asymmetry of S and θ_e in the shear-relative framework is the same as in the storm-motion-relative framework on 15 September (cf. Fig. 10), showing the downshear-right quadrant had the largest enthalpy flux in the eyewall region (Fig. 11a). On 16 September, the storm was moving to the north, while the shear direction was toward the northwest with a difference in angle of 25°. The magnitude of the enthalpy flux on 16 September was much smaller than that on 15 September, as discussed earlier. The upshear-right quadrant had the smallest enthalpy flux on 16 September (Fig. 11b).

In the hurricane eye, the magnitude of θ_e was comparable on 15 and 16 September when the storm intensity was similar (Figs. 11c and 11d). On 15 September, the upshear-left quadrant had the smallest θ_e, while the downshear-right quadrant had the largest θ_e in the region within twice the RMW (Fig. 11c). A similar pattern of asymmetry in θ_e inward from the eyewall ($r^* < 1$) was found on 16 September, but the θ_e was much smaller on the right side of the storm than on the left side of the storm outside the eyewall region (Fig. 11d). The vertical motion at 1-km altitude from the Doppler radar observations collected at the same time during the IRsonde observations is also shown in Figs. 11c and 11d. It appears that the strongest updrafts were located in the downshear-right quadrant, consistent with the composite analysis from Reasor et al. (2013). This strong upward motion was collocated with the large θ_e favoring deep convection, consistent with composite analysis of Zhang et al. (2013). It is also evident from Figs. 11c and 11d that the stronger downdrafts were generally collocated with smaller θ_e, indicating downdrafts bringing low θ_e air into the boundary layer from above. This result provides further evidence of convective or mesoscale downdrafts modulating the boundary layer thermodynamics in the hurricane, in agreement with previous studies (e.g., Powell 1990; Barnes and Powell 1995; Riemer et al. 2010; Molinari et al. 2013; Zhang et al. 2013).

To clearly show the asymmetry of θ_e, the wavenumber 0 plus wavenumber 1 components of θ_e are plotted (Figs. 11e and 11f). Consistent with previous composite analysis given by Zhang et al. (2013), our result shows that near-surface θ_e was the smallest in the upshear-left quadrant and was the largest in the downshear-right quadrant in the eyewall region. This wavenumber 1 asymmetry is slightly clearer on 15 September than on 16 September. As the air moved from the upshear-left quadrant to the downshear right quadrant, θ_e increased as the air experienced surface enthalpy fluxes. A back-of-the-envelope calculation of boundary layer recovery of θ_e suggests that surface enthalpy fluxes were enough to support the recovery of θ_e on 15 September but that they were far from enough to support the recovery of θ_e on 16 September (see details in the appendix). This result further evidences that surface enthalpy fluxes are important for hurricane intensification. Without enough surface fluxes, the energy (θ_e) cannot be recovered from convective downdrafts and thus is insufficient to support deep convection.

4. Conclusions

This study presents an analysis of a new type of expendable instrument (IRsonde) that can be dropped from manned aircraft, complementing the existing dropsonde system with simultaneous SST observations in TCs. The IRsonde-measured SSTs are compared to in situ SSTs observed by AXBTs, showing good agreement, especially for the IRsondes released in rain-free to light rain conditions. The IRsonde data provide a unique opportunity to study the thermodynamic and kinematic structure of the hurricane boundary layer.

IRsonde data collected in Hurricane Edouard (2014) are analyzed to study air–sea interaction processes. Both symmetric and asymmetric surface layer structures are studied using IRsonde data along with AXTB data. The radial variation of the axisymmetric surface temperature and humidity shows a similar trend as in previous studies based on both buoy and dropsonde observations (Cione et al. 2000; Barnes and Bogner 2001). The radial variation of SST suggests the SST cooling is around 2°–3°C on average in the eyewall region of Hurricane Edouard from 15 to 17 September. The SST cooling on 17 September became smaller than the other 2 days as the storm moved into the cold-water region, which is also consistent with the 1D cooling algorithm developed by Cione and Uhlhorn (2003) using extensive buoy data. Asymmetric 2D analysis of the surface layer fields on 15 and 16 September indicates that the SST cooling is the strongest in the right-rear quadrant relative to the storm motion, which is consistent with previous observational and theoretical studies.

Surface enthalpy fluxes are calculated by applying the IRsonde observations to the bulk aerodynamic method. Our results support the notion that SST is an important parameter for regulating the magnitude and distribution of surface fluxes and is tied to storm intensity. The magnitude of the surface enthalpy flux on 15 September when Hurricane Edouard was under intensification was nearly an order of magnitude larger than that on 16 September when Edouard was weakening, although the storm intensity was comparable and the magnitude of environmental wind shear is also similar on these 2 days. It was found that the air–sea thermodynamic equilibrium state determines the magnitude of the surface enthalpy flux during these 2 days.

Estimates of the variation of θ_e showed that the surface enthalpy fluxes were enough to recover low θ_e induced by convective downdrafts from the upshear-left quadrant to the downshear-right quadrant on 15 September, but not on 16 September. Of note, if not recovered by surface fluxes, the boundary layer θ_e would be 4–5 K smaller in the downshear-right quadrant where convection was initiated, according to the simple budget analysis (see the appendix). This result supports the conceptual model of the energy cycle in the eyewall of a sheared TC articulated by Zhang et al. (2013), emphasizing the important role of surface flux–induced boundary layer recovery in regulating the thermodynamic conditions tied to the asymmetry of convection.

This study is the first attempt to explore the role of surface enthalpy fluxes versus the role of the total energy content (θ_e) in that portion of the boundary layer that feeds the hurricane eyewall. Increasing fluxes could certainly contribute to intensification but does a TC require high fluxes to maintain a given intensity? The observations presented here and hinted at in some earlier work support the notion that the moisture fluxes in the eyewall can be much lower than some numerical simulations might assume when the difference in humidity from sea to air decreases markedly. This difference, in turn, is caused by the cooler SST and cooler surface air found there as well as a rise in the relative humidity (RH) in the surface layer. The inflow simply cannot accept much extra latent energy once it approaches saturation (RH > 95%); spray droplets will not evaporate very much either. Above all, our result suggests that while the hurricane intensity is correlated to the θ_e of the inflow more than the surface fluxes, the boundary layer recovery of θ_e through surface fluxes may be a key mechanism for TC intensity change.

Acknowledgments. The authors acknowledge the support from Hurricane Sandy Social Services Block Grant Supplemental Funds (Disaster Relief Appropriations Act, 2013). Jun Zhang was also partially supported by NSF Grant AGS1249732; NOAA Grants NA14NWS4680028, NA14NWS4680030, and NA14OAR4830172; and NASA Grant NNX14AM69G. Evan Kalina held a National Research Council (NRC) Research Associateship Award at the Atlantic Oceanographic and Meteorological Laboratory (AOML) and the Earth System Research Laboratory (ESRL). We thank all of the colleagues from AOC and HRD who participated in the P3 missions into Hurricane Edouard (2014). We are grateful to Sim Aberson for his comments on an earlier version of the paper. We thank Gary Barnes and two anonymous reviewers for their comments, which led to the improvement of our paper.

APPENDIX

Changes in Near-Surface θ_e as a Result of Surface Fluxes

The description of the method and equations for boundary layer recovery calculation parallels those of Zhang et al. (2013). Following Molinari et al. (2013) and Zhang et al. (2013), we estimate the rate of change in θ_e due to sensible and latent heat fluxes at an altitude of 10 m in the eyewall region. Surface enthalpy fluxes are calculated using the bulk method following Eqs. (1) and (2) (cf. Fig. 11).

Changes in potential temperature θ and specific humidity q at a given height caused by surface sensible F_H and latent heat F_q fluxes in the surface layer take the form of

$$\frac{d\theta}{dt} = \frac{\theta}{c_p T}\left(-\frac{1}{\rho}\frac{\partial F_{HZ}}{\partial z}\right) = \frac{\theta}{c_p T}\left(\frac{F_{H0}}{\rho \Delta_Z}\right), \tag{A1}$$

$$\frac{dq}{dt} = \left(\frac{1}{\rho L_v} - \frac{\partial F_{qz}}{\partial z}\right) = \frac{F_{q0}}{\rho L_v \Delta z}, \tag{A2}$$

where the subscript in the flux denotes the height (z represents the height of the measurement and 0 represents the sea surface) and Δz is the boundary layer height. Here F_{H0} and F_{q0} are equivalent to H and E, in Eqs. (1) and (2), respectively. Note that the fluxes are assumed to change linearly with height from the surface to the top of the boundary layer. Taking the inflow layer depth as the boundary layer height following Zhang et al. (2011), Δz is estimated to be ~700 m using the dropsonde data. We note also that the unit of T is in kelvins.

To estimate the θ_e changes caused by the enthalpy fluxes, we first apply a logarithmic differentiation to the θ_e equation shown below,

$$\theta_e = \theta \exp\left(\frac{L_v q}{c_p T_{\mathrm{LCL}}}\right), \tag{A3}$$

to obtain the equation for the rate of change in θ_e. The equation after differentiation has the form of

$$\frac{d\theta_e}{dt} = \frac{\theta_e}{\theta}\frac{d\theta}{dt} + \frac{\theta_e L_v}{c_p T_{\mathrm{LCL}}}\frac{dq}{dt}, \tag{A4}$$

where T_{LCL} is the temperature at the lifting condensation level, which can be calculated following either Bolton (1980) or Davies-Jones (2009).

On 15 September, at a height of 10 m, the mean θ, T, and ρ are 300.3 K, 298.1 K, and 1.14 kg m^{-3}, respectively. Substituting these values along with measured sensible heat and latent heat fluxes into Eqs. (A1) and (A2) gives a change in θ of 0.6 K h^{-1} and a change in q of 1.1 g kg^{-1} h^{-1}. The computed mean values of θ_e, θ, and $T_{\rm LCL}$ are 360 K, 300.3 K, and 297 K, respectively, from the dropsonde data. Of note, variations in these quantities caused by expected errors would not significantly modify the result. Substituting Eqs. (A1)–(A3) into (A4), it is found that θ_e increases at a rate of approximately 3.92 K h^{-1}. For an air parcel to move from the upshear-left (UL) quadrant to the downshear-right (DR) quadrant in the eyewall region (r^*~1), it takes 1.4 h given an RMW of ~35 km and a mean wind speed of 43 m s^{-1}. During this period, θ_e increases 5.55 K, which is much larger than the observed downshear increase in θ_e (~4.5 K). This result suggests that surface enthalpy fluxes are sufficient to produce the observed boundary layer recovery of θ_e.

On 16 September, at a height of 10 m, the mean θ, T, and ρ are 300.4 K, 298.1 K, and 1.14 kg m^{-3}, respectively. Substituting these values along with fluxes into Eqs. (A1) and (A2) gives a θ change of 0.04 K h^{-1} and a q change of 0.28 g kg^{-1} h^{-1}. The computed mean values of θ_e, θ, and $T_{\rm LCL}$ are 360 K, 300.4 K, and 297.3 K, respectively, from the dropsonde data. Substituting these values into Eq. (A4), the result shows that θ_e increases at a rate of approximately 0.87 K h^{-1}. On this day, the strongest θ_e asymmetry is observed at the annulus inward from the RMW (r^* ~0.5) to the storm center. For an air parcel to travel from the UL quadrant to the DR quadrant in the eyewall region (r^*~0.5), it takes 43 min given an RMW of ~27 km and a mean wind speed of 36.6 m s^{-1}. During this period, θ_e increases 0.62 K, which is much smaller than the observed downshear increase in θ_e (~2 K), suggesting that surface enthalpy fluxes are not sufficient to produce the observed boundary layer recovery of θ_e. In the outer radii outside the eyewall, for an air parcel to travel from the location of lowest θ_e (right quadrant) to that of the highest θ_e (left quadrant), it takes a much longer time (~100 min) at a mean wind speed of 30 m s^{-1}. During this period, θ_e increases 1.5 K, which is much smaller than the observed downshear increase in θ_e (~3K), again suggesting that surface enthalpy fluxes are not sufficient to produce the observed boundary layer recovery.

Of note, the effects of dissipative heating and eye–eyewall mixing are not included in the abovementioned boundary layer recovery calculation (Bister and Emanuel 1998; Zhang 2010b; Eastin et al. 2005), which parallels those in Zhang et al. (2013) and Molinari et al. (2013). Equations (A1) and (A2) also neglect the entrainment effect near the top of the boundary layer. Nonetheless, our estimates are similar to a more complex calculation used by Wroe and Barnes (2003).

REFERENCES

Barnes, G. M., and M. D. Powell, 1995: Evolution of the inflow boundary layer of Hurricane Gilbert (1988). *Mon. Wea. Rev.*, **123**, 2348–2368, doi:10.1175/1520-0493(1995)123<2348:EOTIBL>2.0.CO;2.

——, and P. B. Bogner, 2001: Comments on "Surface observations in the hurricane environment." *Mon. Wea. Rev.*, **129**, 1267–1269, doi:10.1175/1520-0493(2001)129<1267:COSOIT>2.0.CO;2.

Bell, M. M., M. T. Montgomery, and K. A. Emanuel, 2012: Air–sea enthalpy and momentum exchange at major hurricane wind speeds observed during CBLAST. *J. Atmos. Sci.*, **69**, 3197–3222, doi:10.1175/JAS-D-11-0276.1.

Bender, M. A., I. Ginis, R. Tuleya, B. Thomas, and T. Marchok, 2007: The operational GFDL coupled hurricane–ocean prediction system and a summary of its performance. *Mon. Wea. Rev.*, **135**, 3965–3989, doi:10.1175/2007MWR2032.1.

Bister, M., and K. A. Emanuel, 1998: Dissipative heating and hurricane intensity. *Meteor. Atmos. Phys.*, **65**, 233–240, doi:10.1007/BF01030791.

Black, P. G., and Coauthors, 2007: Air–sea exchange in hurricanes: Synthesis of observations from the Coupled Boundary Layer Air–Sea Transfer Experiment. *Bull. Amer. Meteor. Soc.*, **88**, 357–374, doi:10.1175/BAMS-88-3-357.

——, L. Harrison, M. Beaubien, R. Bluth, R. Woods, A. Penny, R. W. Smith, and J. D. Doyle, 2017: High-definition Sounding System (HDSS) for atmospheric profiling. *J. Atmos. Oceanic Technol.*, **34**, 777–796, doi:10.1175/JTECH-D-14-00210.1.

Bolton, D., 1980: The computation of equivalent potential temperature. *Mon. Wea. Rev.*, **108**, 1046–1053, doi:10.1175/1520-0493(1980)108<1046:TCOEPT>2.0.CO;2.

Braun, S. A., and W.-K. Tao, 2000: Sensitivity of high-resolution simulations of Hurricane Bob (1991) to planetary boundary layer parameterizations. *Mon. Wea. Rev.*, **128**, 3941–3961, doi:10.1175/1520-0493(2000)129<3941:SOHRSO>2.0.CO;2.

Bryan, G. H., 2012: Effects of surface exchange coefficients and turbulence length scales on the intensity and structure of numerically simulated hurricanes. *Mon. Wea. Rev.*, **140**, 1125–1143, doi:10.1175/MWR-D-11-00231.1.

Byers, H. R., 1944: *General Meteorology*. 2nd ed. McGraw Hill, 645 pp.

Chen, S. S., J. F. Price, W. Zhao, M. A. Donelan, and E. J. Walsh, 2007: The CBLAST Hurricane Program and the next-generation fully coupled atmosphere–wave–ocean models for hurricane research and prediction. *Bull. Amer. Meteor. Soc.*, **88**, 311–317, doi:10.1175/BAMS-88-3-311.

Cione, J. J., 2015: The relative roles of the ocean and atmosphere as revealed by buoy air–sea observations in hurricanes. *Mon. Wea. Rev.*, **143**, 904–913, doi:10.1175/MWR-D-13-00380.1.

——, and E. W. Uhlhorn, 2003: Sea surface temperature variability in hurricanes: Implications with respect to intensity change. *Mon. Wea. Rev.*, **131**, 1783–1796, doi:10.1175//2562.1.

——, P. Black, and S. Houston, 2000: Surface observations in the hurricane environment. *Mon. Wea. Rev.*, **128**, 1550–1561, doi:10.1175/1520-0493(2000)128<1550:SOITHE>2.0.CO;2.

——, E. A. Kalina, J. Zhang, and E. Uhlhorn, 2013: Observations of air–sea interaction and intensity change in hurricanes. *Mon. Wea. Rev.*, **141**, 2368–2382, doi:10.1175/MWR-D-12-00070.1.

D'Asaro, E. A., T. B. Sanford, P. P. Niiler, and E. J. Terrill, 2007: Cold wake of Hurricane Frances. *Geophys. Res. Lett.*, **34**, L15609, doi:10.1029/2007GL030160.

Davies-Jones, R., 2009: On formulas for equivalent potential temperature. *Mon. Wea. Rev.*, **137**, 3137–3148, doi:10.1175/2009MWR2774.1.

Davis, C., and Coauthors, 2008: Prediction of landfalling hurricanes with the Advanced Hurricane WRF model. *Mon. Wea. Rev.*, **136**, 1990–2005, doi:10.1175/2007MWR2085.1.

DeMaria, M., M. Mainelli, L. K. Shay, J. A. Knaff, and J. Kaplan, 2005: Further improvements to the Statistical Hurricane Intensity Prediction Scheme (SHIPS). *Wea. Forecasting*, **20**, 531–543, doi:10.1175/WAF862.1.

Dolling, K., and G. M. Barnes, 2014: The evolution of Hurricane Humberto (2001). *Mon. Wea. Rev.*, **71**, 1276–1291, doi:10.1175/JAS-D-13-0164.1.

Drennan, W. M., J. A. Zhang, J. R. French, C. McCormick, and P. G. Black, 2007: Turbulent fluxes in the hurricane boundary layer. Part II: Latent heat flux. *J. Atmos. Sci.*, **64**, 1103–1115, doi:10.1175/JAS3889.1.

Eastin, M. D., W. M. Gray, and P. G. Black, 2005: Buoyancy of convective vertical motions in the inner core of intense hurricanes. Part II: Case studies. *Mon. Wea. Rev.*, **133**, 209–227, doi:10.1175/MWR-2849.1.

Emanuel, K. A., 1986: An air–sea interaction theory for tropical cyclones. Part I: Steady-state maintenance. *J. Atmos. Sci.*, **43**, 585–605, doi:10.1175/1520-0469(1986)043<0585:AASITF>2.0.CO;2.

——, 1988: The maximum intensity of hurricanes. *J. Atmos. Sci.*, **45**, 1143–1155, doi:10.1175/1520-0469(1988)045<1143:TMIOH>2.0.CO;2.

——, 1995: Sensitivity of tropical cyclones to surface exchange coefficients and a revised steady-state model incorporating eye dynamics. *J. Atmos. Sci.*, **52**, 3969–3976, doi:10.1175/1520-0469(1995)052<3969:SOTCTS>2.0.CO;2.

French, J. R., W. M. Drennan, J. A. Zhang, and P. G. Black, 2007: Turbulent fluxes in the hurricane boundary layer. Part I: Momentum flux. *J. Atmos. Sci.*, **64**, 1089–1102, doi:10.1175/JAS3887.1.

Green, B. W., and F. Zhang, 2014: Sensitivity of tropical cyclone simulations to parametric uncertainties in air–sea fluxes and implications for parameter estimation. *Mon. Wea. Rev.*, **142**, 2290–2308, doi:10.1175/MWR-D-13-00208.1.

Halliwell, G. R., S. Gopalakrishnan, F. Marks, and D. Willey, 2015: Idealized study of ocean impacts on tropical cyclone intensity forecasts. *Mon. Wea. Rev.*, **143**, 1142–1165, doi:10.1175/MWR-D-14-00022.1.

Haus, B. K., D. Jeong, M. A. Donelan, J. A. Zhang, and I. Savelyev, 2010: Relative rates of sea air heat transfer and frictional drag in very high winds. *Geophys. Res. Lett.*, **37**, L07802, doi:10.1029/2009GL042206.

Hock, T., 2014: AVAPS II infrared sea surface skin temperature. NCAR Tech. Note, 11 pp.

Jaimes, B., and L. K. Shay, 2009: Mixed layer cooling in mesoscale ocean eddies during Hurricanes Katrina and Rita. *Mon. Wea. Rev.*, **137**, 4188–4207, doi:10.1175/2009MWR2849.1.

——, ——, and E. W. Uhlhorn, 2015: Enthalpy and momentum fluxes during Hurricane Earl relative to underlying ocean features. *Mon. Wea. Rev.*, **143**, 111–131, doi:10.1175/MWR-D-13-00277.1.

Kaplan, J., and Coauthors, 2015: Evaluating environmental impacts on tropical cyclone rapid intensification predictability utilizing statistical models. *Wea. Forecasting*, **30**, 1374–1396, doi:10.1175/WAF-D-15-0032.1.

Kepert, J. D., and Y. Wang, 2001: The dynamics of boundary layer jets within the tropical cyclone core. Part II: Nonlinear enhancement. *J. Atmos. Sci.*, **58**, 2485–2501, doi:10.1175/1520-0469(2001)058<2485:TDOBLJ>2.0.CO;2.

Kim, H.-S., C. Lozano, V. Tallapragada, D. Iredell, D. Sheinin, H. L. Tolman, V. M. Gerald, and J. Sims, 2014: Performance of ocean simulations in the coupled HWRF–HYCOM model. *J. Atmos. Oceanic Technol.*, **31**, 545–559, doi:10.1175/JTECH-D-13-00013.1.

Knaff, J. A., M. DeMaria, C. R. Sampson, J. E. Peak, J. Cummings, and W. H. Schubert, 2013: Upper oceanic energy response to tropical cyclone passage. *J. Climate*, **26**, 2631–2650, doi:10.1175/JCLI-D-12-00038.1.

Lin, I.-I., C.-C. Wu, K. A. Emanuel, I.-H. Lee, C.-R. Wu, and I.-F. Pun, 2005: The interaction of Supertyphoon Maemi with a warm ocean eddy. *Mon. Wea. Rev.*, **133**, 2635–2649, doi:10.1175/MWR3005.1.

——, C.-H. Chen, I.-F. Pun, W. T. Liu, and C.-C. Wu, 2009a: Warm ocean anomaly, air–sea fluxes, and the rapid intensification of Tropical Cyclone Nargis (2008). *Geophys. Res. Lett.*, **36**, L03817, doi:10.1029/2008GL035815.

——, I.-F. Pun, and C.-C. Wu, 2009b: Upper-ocean thermal structure and the western North Pacific category 5 typhoons. Part II: Dependence on translation speed. *Mon. Wea. Rev.*, **137**, 3744–3757, doi:10.1175/2009MWR2713.1.

Malkus, J. S., and H. Riehl, 1960: On the dynamics and energy transformations in steady-state hurricanes. *Tellus*, **12**, 1–20, doi:10.3402/tellusa.v12i1.9351.

Miller, B. I., 1958: On the maximum intensity of hurricanes. *J. Meteor.*, **15**, 184–195, doi:10.1175/1520-0469(1958)015<0184:OTMIOH>2.0.CO;2.

Ming, J., and J. A. Zhang, 2016: Effects of surface flux parameterization on the numerically simulated intensity and structure of Typhoon Morakot (2009). *Adv. Atmos. Sci.*, **33**, 58–72, doi:10.1007/s00376-015-4202-z.

Molinari, J., J. Frank, and D. Vollaro, 2013: Convective bursts, downdraft cooling, and boundary layer recovery in a sheared tropical storm. *Mon. Wea. Rev.*, **141**, 1048–1060, doi:10.1175/MWR-D-12-00135.1.

Moss, M. S., 1978: Low-level turbulence structure in the vicinity of a hurricane. *Mon. Wea. Rev.*, **106**, 841–849, doi:10.1175/1520-0493(1978)106<0841:LLTSIT>2.0.CO;2.

——, and F. J. Merceret, 1976: A note on several low-layer features of Hurricane Eloise (1975). *Mon. Wea. Rev.*, **104**, 967–971, doi:10.1175/1520-0493(1976)104<0967:ANOSLL>2.0.CO;2.

Nolan, D. S., J. A. Zhang, and D. P. Stern, 2009a: Evaluation of planetary boundary layer parameterizations in tropical cyclones by comparison of in situ data and high-resolution simulations of Hurricane Isabel (2003). Part I: Initialization, maximum winds, and outer core boundary layer structure. *Mon. Wea. Rev.*, **137**, 3651–3674, doi:10.1175/2009MWR2785.1.

——, D. P. Stern, and J. A. Zhang, 2009b: Evaluation of planetary boundary layer parameterizations in tropical cyclones by comparison of in situ data and high-resolution simulations of Hurricane Isabel (2003). Part II: Inner-core boundary layer and eyewall structure. *Mon. Wea. Rev.*, **137**, 3675–3698, doi:10.1175/2009MWR2786.1.

Palmen, E., 1948: On the formation and structure of tropical cyclones. *Geophysica*, **3**, 184–195.

Powell, M. D., 1990: Boundary layer structure and dynamics in outer hurricane rainbands. Part II: Downdraft modification and mixed layer recovery. *Mon. Wea. Rev.*, **118**, 918–938, doi:10.1175/1520-0493(1990)118<0918:BLSADI>2.0.CO;2.

Price, J. F., 1981: Upper ocean response to a hurricane. *J. Phys. Oceanogr.*, **11**, 153–175, doi:10.1175/1520-0485(1981)011<0153:UORTAH>2.0.CO;2.

——, T. B. Sanford, and G. Z. Forristall, 1994: Forced stage response to a moving hurricane. *J. Phys. Oceanogr.*, **24**, 233–260, doi:10.1175/1520-0485(1994)024<0233:FSRTAM>2.0.CO;2.

Reasor, R. P., R. Rogers, and S. Lorsolo, 2013: Environmental flow impacts on tropical cyclone structure diagnosed from airborne Doppler radar composites. *Mon. Wea. Rev.*, **141**, 2949–2969, doi:10.1175/MWR-D-12-00334.1.

Riemer, M., M. T. Montgomery, and M. E. Nicholls, 2010: A new paradigm for intensity modification of tropical cyclones: Thermodynamic impact of vertical wind shear on the inflow layer. *Atmos. Chem. Phys.*, **10**, 3163–3188, doi:10.5194/acp-10-3163-2010.

Rogers, R. F., P. D. Reasor, and J. A. Zhang, 2015: Multiscale structure and evolution of Hurricane Earl (2010) during rapid intensification. *Mon. Wea. Rev.*, **143**, 536–562, doi:10.1175/MWR-D-14-00175.1.

——, J. A. Zhang, J. Zawislak, H. Jiang, G. R. Alvey III, E. J. Zipser, and S. N. Stevenson, 2016: Observations of the structure and evolution of Hurricane Edouard (2014) during intensity change. Part II: Kinematic structure and distribution of deep convection. *Mon. Wea. Rev.*, **144**, 3355–3376, doi:10.1175/MWR-D-16-0017.1.

Schneider, R., and G. M. Barnes, 2005: Low-level kinematic, thermodynamic, and reflectivity fields associated with Hurricane Bonnie (1998) at landfall. *Mon. Wea. Rev.*, **133**, 3243–3259, doi:10.1175/MWR3027.1.

Shay, L. K., P. G. Black, A. J. Mariano, J. D. Hawkins, and R. L. Elsberry, 1992: Upper ocean response to hurricane Gilbert. *J. Geophys. Res.*, **97**, 20 227–20 248, doi:10.1029/92JC01586.

——, G. J. Goni, and P. G. Black, 2000: Effects of a warm oceanic feature on Hurricane Opal. *Mon. Wea. Rev.*, **128**, 1366–1383, doi:10.1175/1520-0493(2000)128<1366:EOAWOF>2.0.CO;2.

Shapiro, L. J., 1983: The asymmetric boundary layer flow under a translating hurricane. *J. Atmos. Sci.*, **40**, 1984–1998, doi:10.1175/1520-0469(1983)040<1984:TABLFU>2.0.CO;2.

Sitkowski, M., and G. M. Barnes, 2009: Low-level thermodynamic, kinematic, and reflectivity fields of Hurricane Guillermo (1997) during rapid intensification. *Mon. Wea. Rev.*, **137**, 645–663, doi:10.1175/2008MWR2531.1.

Smith, R. K., and G. L. Thomsen, 2010: Dependence of tropical-cyclone intensification on the boundary-layer representation in a numerical model. *Quart. J. Roy. Meteor. Soc.*, **136**, 1671–1685, doi:10.1002/qj.687.

Stewart, S. R., 2014: National Hurricane Center tropical cyclone report for Hurricane Edouard (AL062014). National Hurricane Center Rep., 19 pp. [Available online at http://www.nhc.noaa.gov/data/tcr/AL062014_Edouard.pdf.]

Uhlhorn, E. W., and L. K. Shay, 2008: Loop current mixed layer energy response to Hurricane Lili (2002). Part I: Observations. *Mon. Wea. Rev.*, **42**, 400–419, doi:10.1175/JPO-D-11-096.1.

——, B. W. Klotz, T. Vukicevic, P. Reasor, and R. F. Rogers, 2014: Observed hurricane wind speed asymmetries and relationships to motion and environmental shear. *Mon. Wea. Rev.*, **142**, 1290–1311, doi:10.1175/MWR-D-13-00249.1.

Wroe, D. R., and G. M. Barnes, 2003: Inflow layer energetics of Hurricane Bonnie (1998) near landfall. *Mon. Wea. Rev.*, **131**, 1600–1612, doi:10.1175//2547.1.

Wu, C.-C., C.-Y. Lee, and I.-I. Lin, 2007: The effect of the ocean eddy on tropical cyclone intensity. *J. Atmos. Sci.*, **64**, 3562–3578, doi:10.1175/JAS4051.1.

Wu, C.-R., Y.-L. Chang, L.-Y. Oey, C.-W. J. Chang, and Y.-C. Hsin, 2008: Air–sea interaction between tropical cyclone Nari and Kuroshio. *Geophys. Res. Lett.*, **35**, L12605, doi:10.1029/2008GL033942.

Yablonsky, R. M., and I. Ginis, 2009: Limitation of one-dimensional ocean models for coupled ocean–hurricane model forecasts. *Mon. Wea. Rev.*, **137**, 4410–4419, doi:10.1175/2009MWR2863.1.

Zawislak, J., H. Jiang, G. R. Alvey III, E. J. Zipser, R. F. Rogers, J. A. Zhang, and S. N. Stevenson, 2016: Observations of the structure and evolution of Hurricane Edouard (2014) during intensity change. Part I: Relationship between the thermodynamic structure and precipitation. *Mon. Wea. Rev.*, **144**, 3333–3354, doi:10.1175/MWR-D-16-0018.1.

Zhang, J. A., 2010a: Spectra characteristics of turbulence in the hurricane boundary layer. *Quart. J. Roy. Meteor. Soc.*, **136**, 918–926. doi:10.1002/qj.610.

——, 2010b: Estimation of dissipative heating using low-level in situ aircraft observations in the hurricane boundary layer. *J. Atmos. Sci.*, **67**, 1853–1862, doi:10.1175/2010JAS3397.1.

——, and E. W. Uhlhorn, 2012: Hurricane sea surface inflow angle and an observation-based parametric model. *Mon. Wea. Rev.*, **140**, 3587–3605, doi:10.1175/MWR-D-11-00339.1.

——, P. G. Black, J. R. French, and W. M. Drennan, 2008: First direct measurements of enthalpy flux in the hurricane boundary layer: The CBLAST results. *Geophys. Res. Lett.*, **35**, L14813, doi:10.1029/2008GL034374.

——, F. D. Marks, M. T. Montgomery, and S. Lorsolo, 2011: An estimation of turbulent characteristics in the low-level region of intense Hurricanes Allen (1980) and Hugo (1989). *Mon. Wea. Rev.*, **139**, 1447–1462, doi:10.1175/2010MWR3435.1.

——, R. F. Rogers, P. Reasor, E. Uhlhorn, and F. D. Marks, 2013: Asymmetric hurricane boundary layer structure from dropsonde composites in relation to the environmental vertical wind shear. *Mon. Wea. Rev.*, **141**, 3968–3984, doi:10.1175/MWR-D-12-00335.1.

——, D. S. Nolan, R. F. Rogers, and V. Tallapragada, 2015: Evaluating the impact of improvements in the boundary layer parameterizations on hurricane intensity and structure forecasts in HWRF. *Mon. Wea. Rev.*, **143**, 3136–3154, doi:10.1175/MWR-D-14-00339.1.

Zhu, T., and D. Zhang, 2006: The impact of the storm-induced SST cooling on hurricane intensity. *Adv. Atmos. Sci.*, **23**, 14–22, doi:10.1007/s00376-006-0002-9.